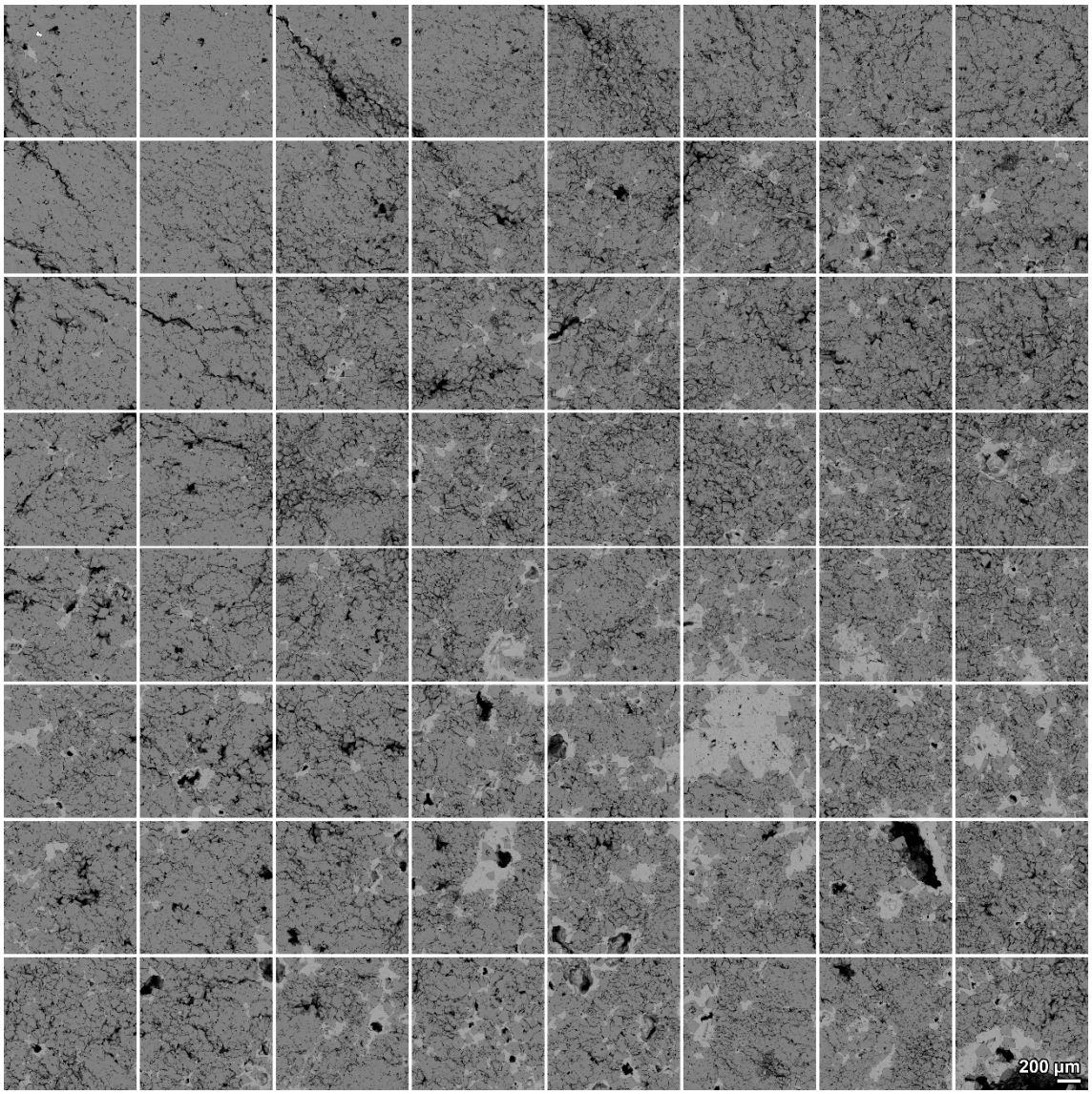

Figure S1a. Fabric-destructive dolomite in CDF07. Backscattered-electron (BSE) images of CDF07, in which replacive dolomite crystals obliterate the original carbonate fabric, so that grains and matrix can no longer be distinguished. The 64 adjacent tiles (8 × 8; each 1.14 × 1.14 mm) are shown in their acquisition positions; narrow strips (~20 µm) along tile boundaries were omitted to remove stitching artefacts. Scale bar (200 µm) applies to all tiles.

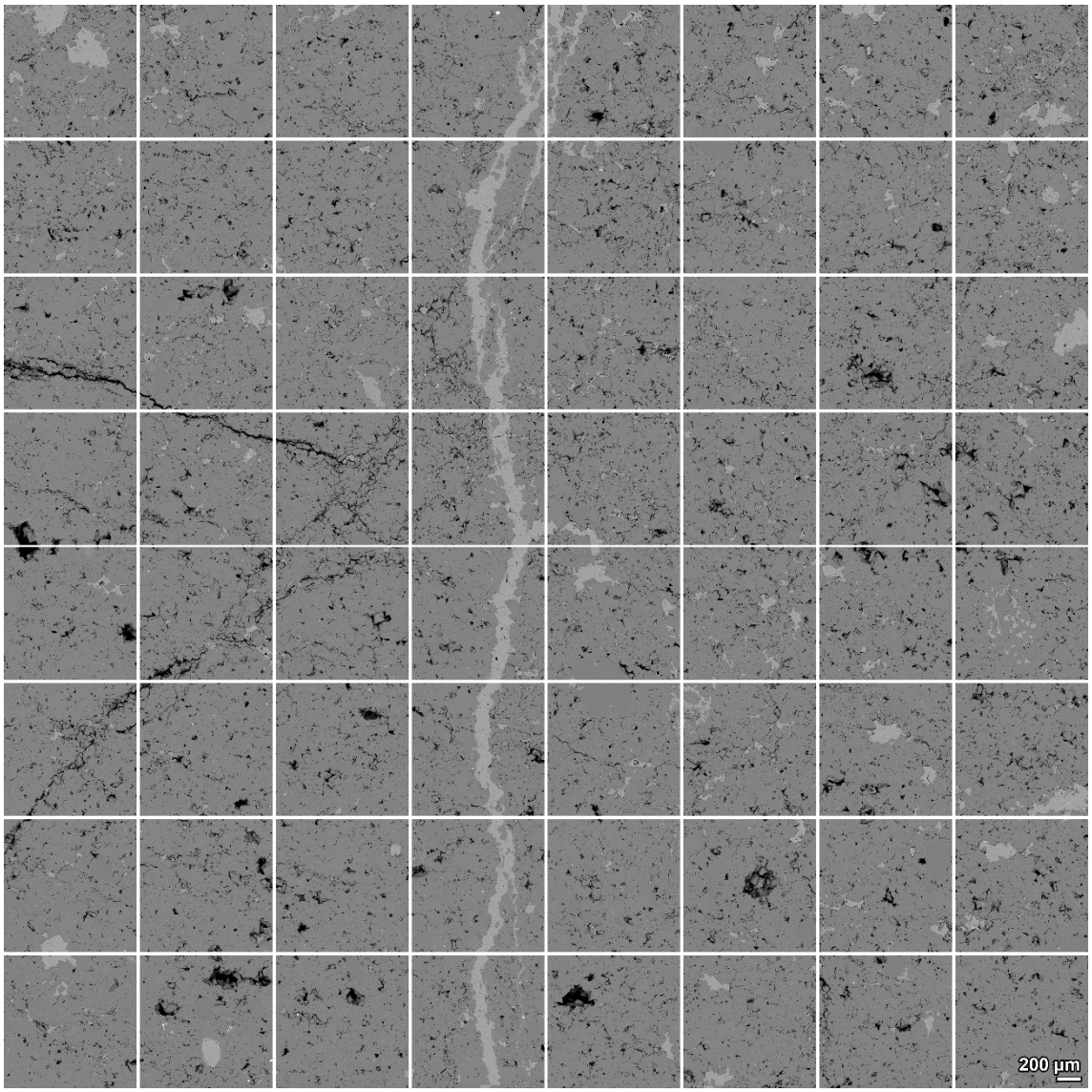

Figure S1b. Fabric-destructive dolomite in the CDF01. Backscattered-electron (BSE) images of CDF01, in which replacive dolomite crystals obliterate the original carbonate fabric, so that grains and matrix can no longer be distinguished. The mosaic is shown as 64 adjacent fields (8 × 8; each 1.14 × 1.14 mm) in their original positions. Scale bar (200 µm) applies to all fields.

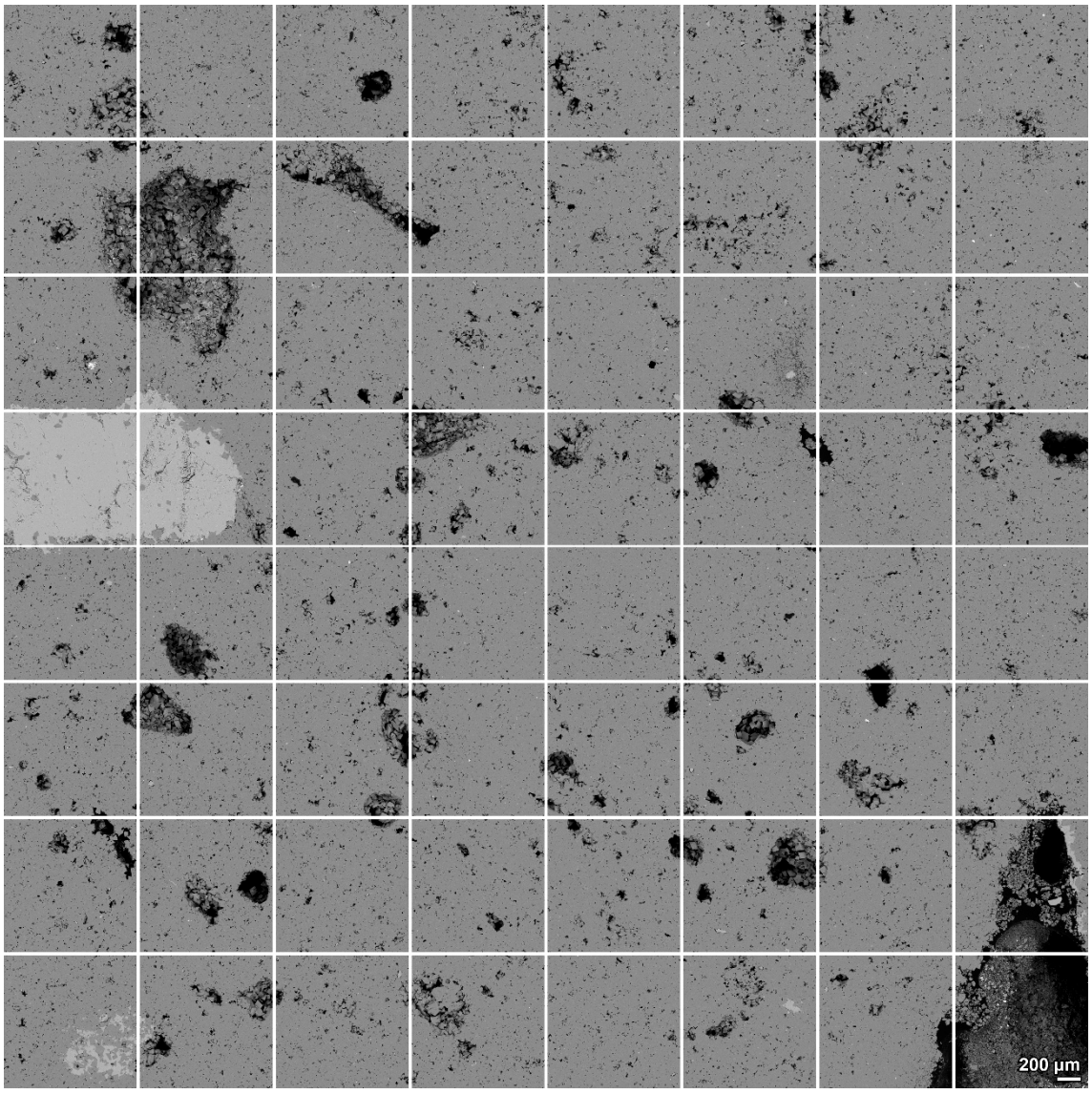

Figure S1c. Fabric-destructive dolomite in the CDF08. Backscattered-electron (BSE) images of CDF08, in which replacive dolomite crystals obliterate the original carbonate fabric, so that grains and matrix can no longer be distinguished. The mosaic is shown as 64 adjacent fields (8 × 8; each 1.14 × 1.14 mm) in their original positions. Scale bar (200 µm) applies to all fields.

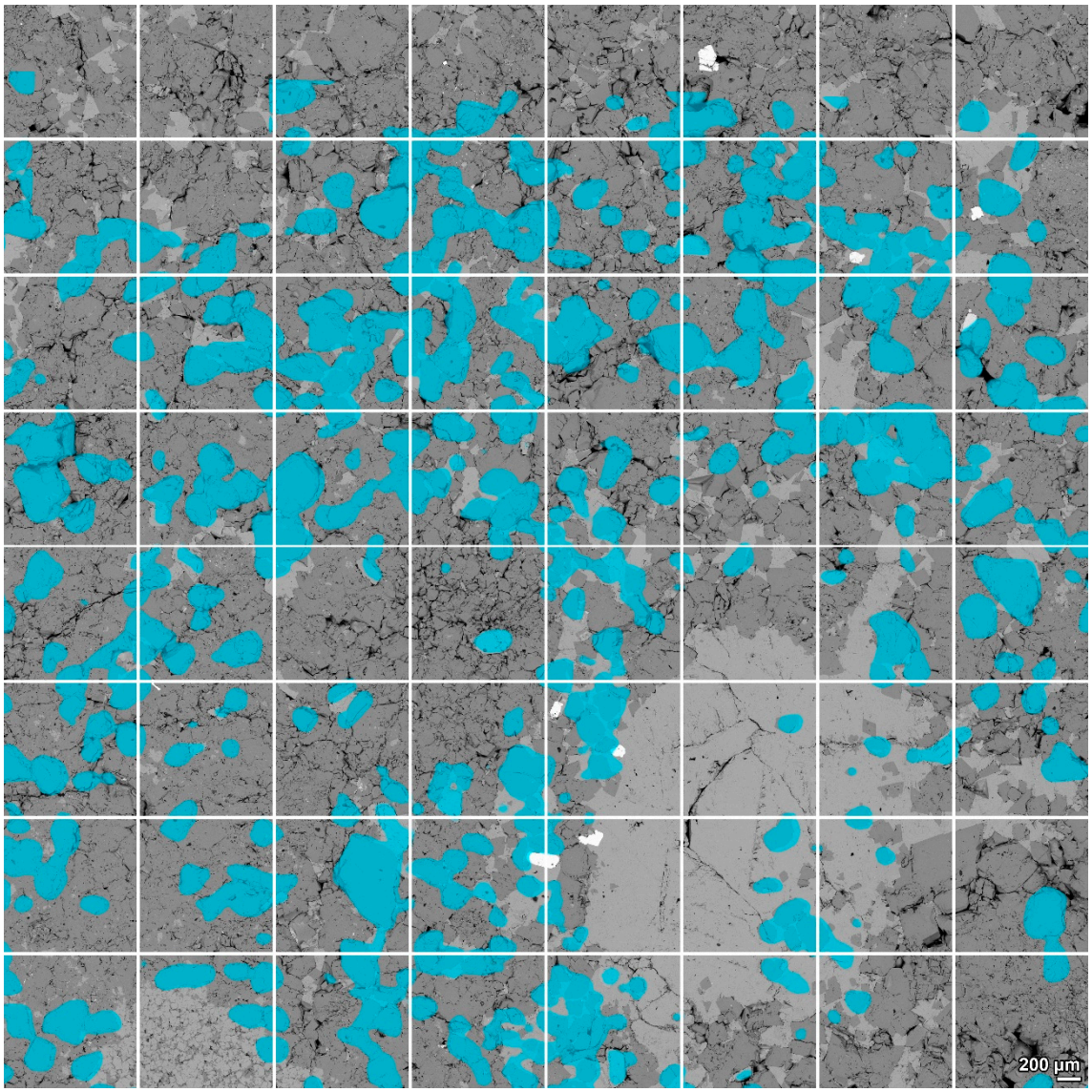

Figure S1d. Quartz in the MCSF configuration MCSF07. BSE mosaic shown as 64 adjacent fields (8 × 8; each 1.14 × 1.14 mm) in their original positions, with quartz (cyan) from the µ-EDXRF Si map (25 µm pixel) registered to the BSE mosaic using the µ-EDXRF Ca map (residual misfit ≈ 20 µm). Quartz ($\bar{Z} \approx 10.8$) and dolomite ($\bar{Z} \approx 10.9$) have nearly identical mean atomic numbers and cannot be distinguished by BSE contrast alone. Scale bar (200 µm) applies to all fields.

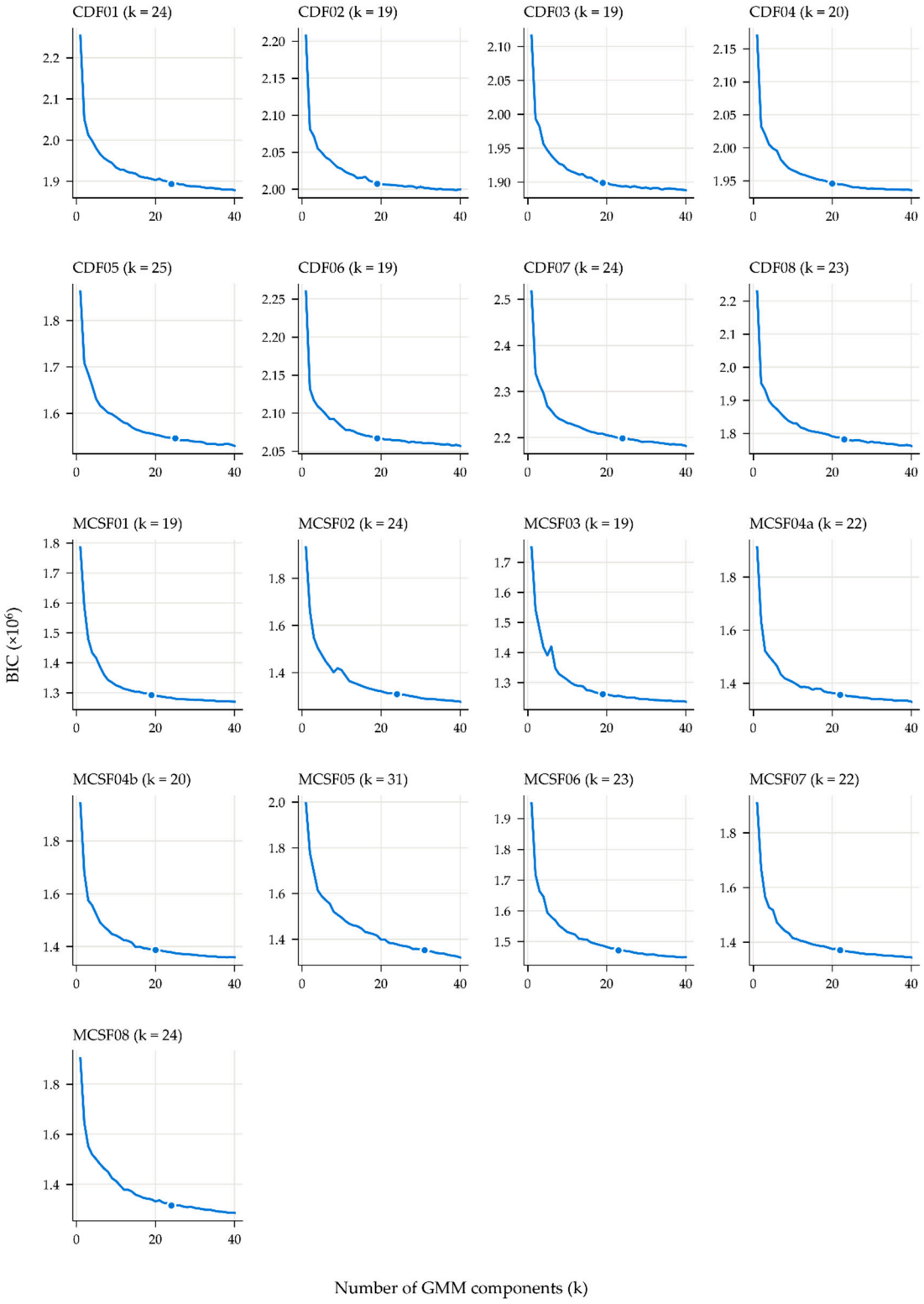

Figure S2. BIC curves of the GMM fits (k = 1–40) for the 17 configurations. The selected number of components, k^*, is the smallest k that reaches 95% of the total decrease of the BIC (Section 3.6, Step 4). In MCSF02, MCSF03, MCSF04b, MCSF05, MCSF07 and MCSF08, the BIC continued to decrease at k = 40, and k^* marks the point of diminishing returns rather than a minimum.

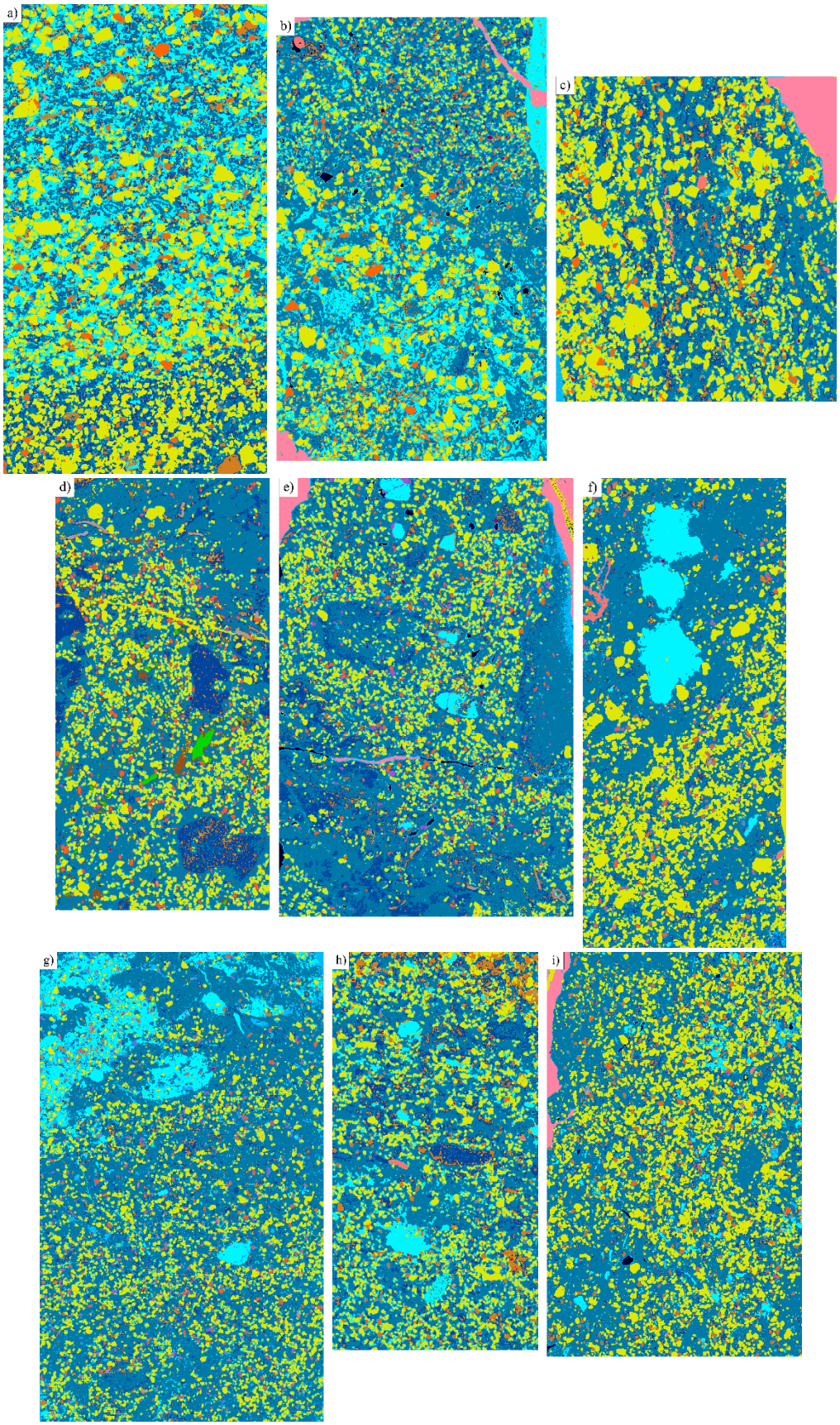

Figure S3a. Full maps of mineral classes and dolomite sub-domains of the MCSF configurations; Figure 5 shows 18 × 18 mm windows of these maps. Dolomite sub-domains are defined in Table 1 and are grouped with dolomite in quantification. Colours as in the legend; scale bar in each panel.

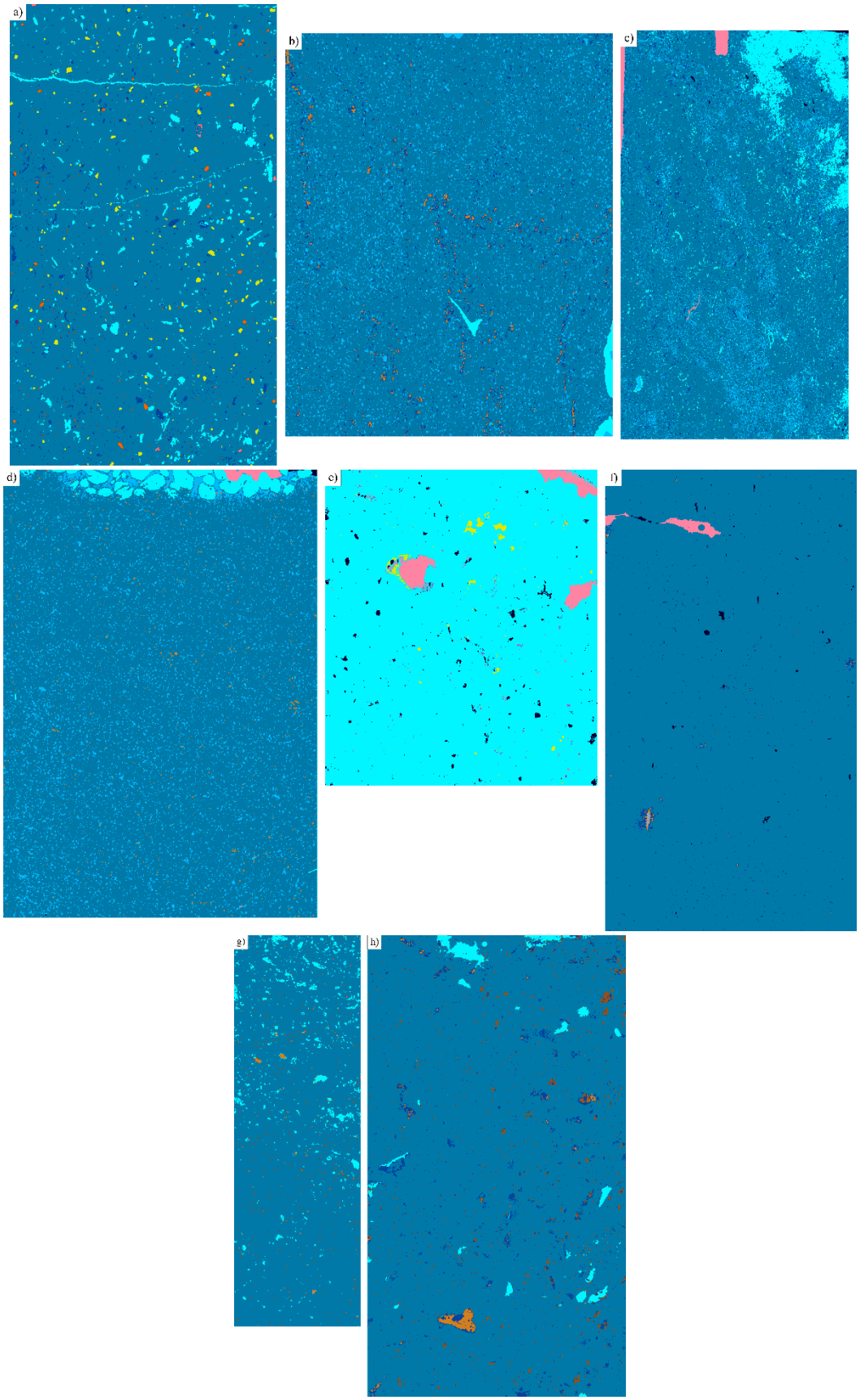

Figure S3b. Full maps of mineral classes and dolomite sub-domains of the CDF configurations; Figure 6 shows 18 × 18 mm windows of these maps. Dolomite sub-domains are defined in Table 1 and are grouped with dolomite in quantification. Colours as in the legend; scale bar in each panel.

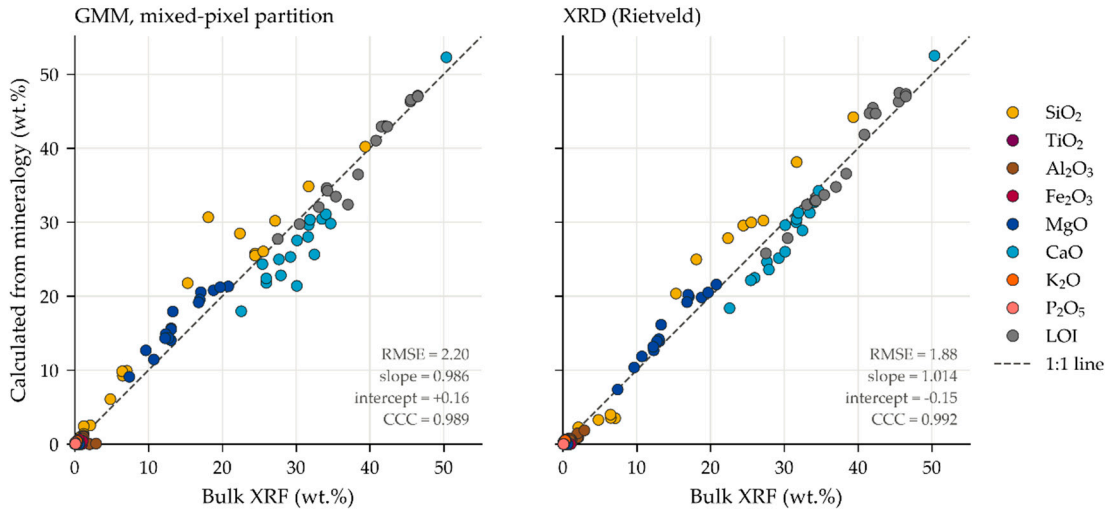

Figure S4. Oxide compositions calculated from (a) the GMM abundances and (b) the XRD/Rietveld abundances, assuming ideal mineral stoichiometry, against the bulk XRF analyses (153 oxide–configuration pairs). Pooled RMSE: (a) 2.20 wt. % (95% CI 1.54–2.88 wt. %; CCC 0.989) and (b) 1.88 wt. % (CCC 0.992). The dashed line is the 1:1 line. MgO plots above and CaO below the 1:1 line in both panels, which is consistent with a Ca-rich dolomite (Section 5.1).

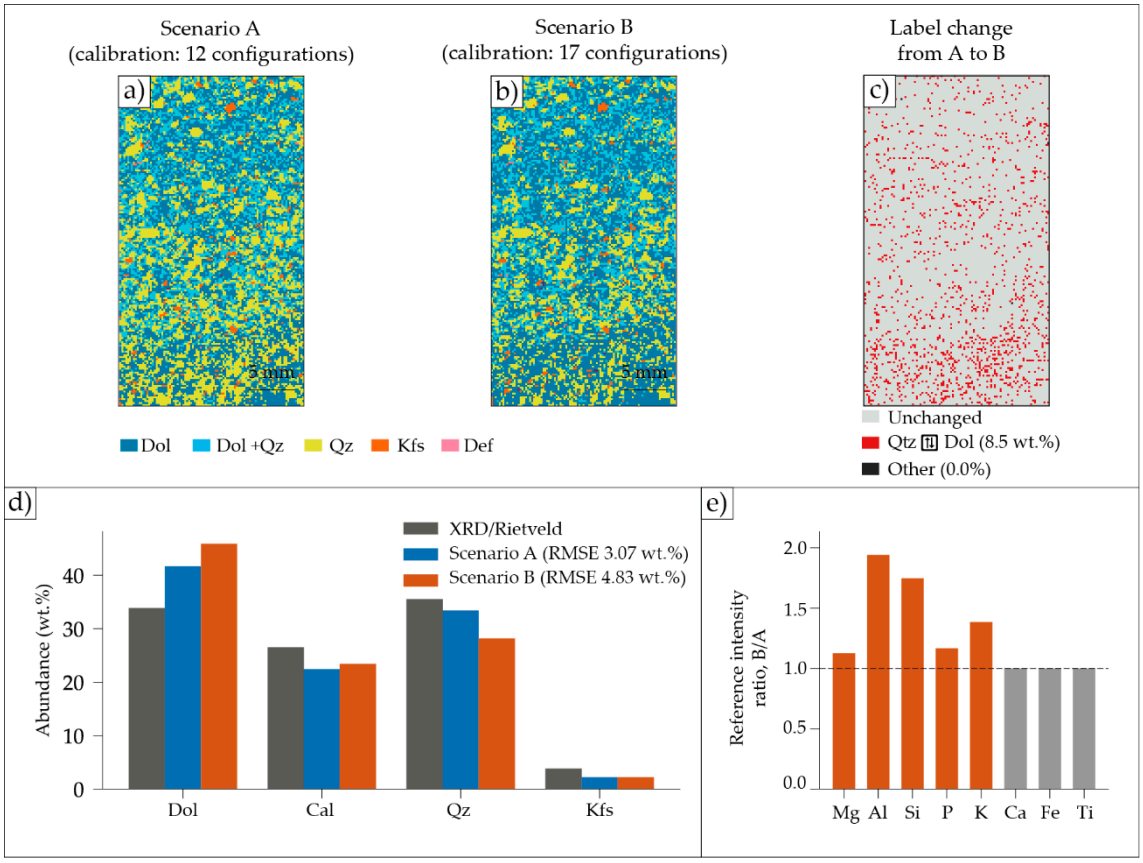

Figure S5. Effect of the calibration set on the maps of MCSF03. The same GMM fit labelled with the reference intensities of (a) scenario A (12 calibration configurations) and (b) scenario B (all 17 configurations). The higher Si reference intensity of scenario B lowers the quartz fraction of every component, so that part of the quartz grains is labelled as dolomite and the RMSE rises from 4.44 to 7.95 wt.%.

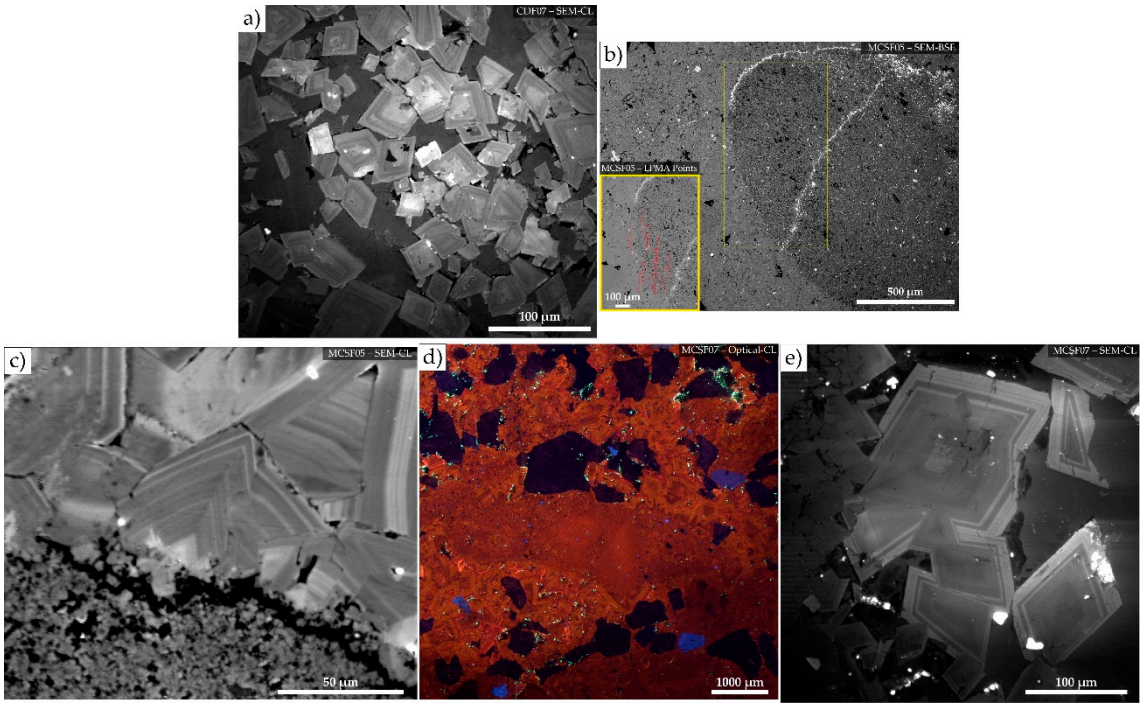

Figure S6. Dolomite and dolomitized bioclasts in BSE and cathodoluminescence images. (a) SEM cathodoluminescence (SEM-CL) intensity image of CDF07: dolomite rhombs with concentric zoning; EPMA analyses of this sample gave near-stoichiometric cores (52.2 mol% $CaCO_3$) and Ca-rich rims (54.3 mol%; Table S8). (b) BSE image of MCSF05: a dolomitized bioclast (right) in contact with blocky dolomite cement (left); bright grains a few micrometres across line the bioclast margin. The yellow box marks the area of (c); the inset shows the EPMA points in the bioclast and in the cement (Table S8). (c) SEM-CL of the same area: fine concentric bands in the blocky cement and weaker, mottled luminescence in the microcrystalline bioclast. (d) Optical cathodoluminescence of MCSF07: dull, homogeneous red dolomitized bioclasts in concentrically zoned orange-red dolomite cement; detrital grains are non-luminescent. (e) SEM-CL of MCSF07: dolomite rhombs with fine concentric bands. SEM-CL images were acquired at the CRTI (Goiânia, Brazil) on a Tescan Amber-X field-emission SEM with a Delmic SPARC detector (panchromatic, 10 kV, 5 nA, , dwell time of 550 µs per pixel). The BSE image in (b) was acquired at CETEM on a Zeiss Sigma 300 VP field-emission SEM. Optical cathodoluminescence: cold-cathode CITL unit on a Zeiss Axio Imager M2m reflected-light microscope, 2.5× objective (Museu Nacional, Universidade Federal do Rio de Janeiro).

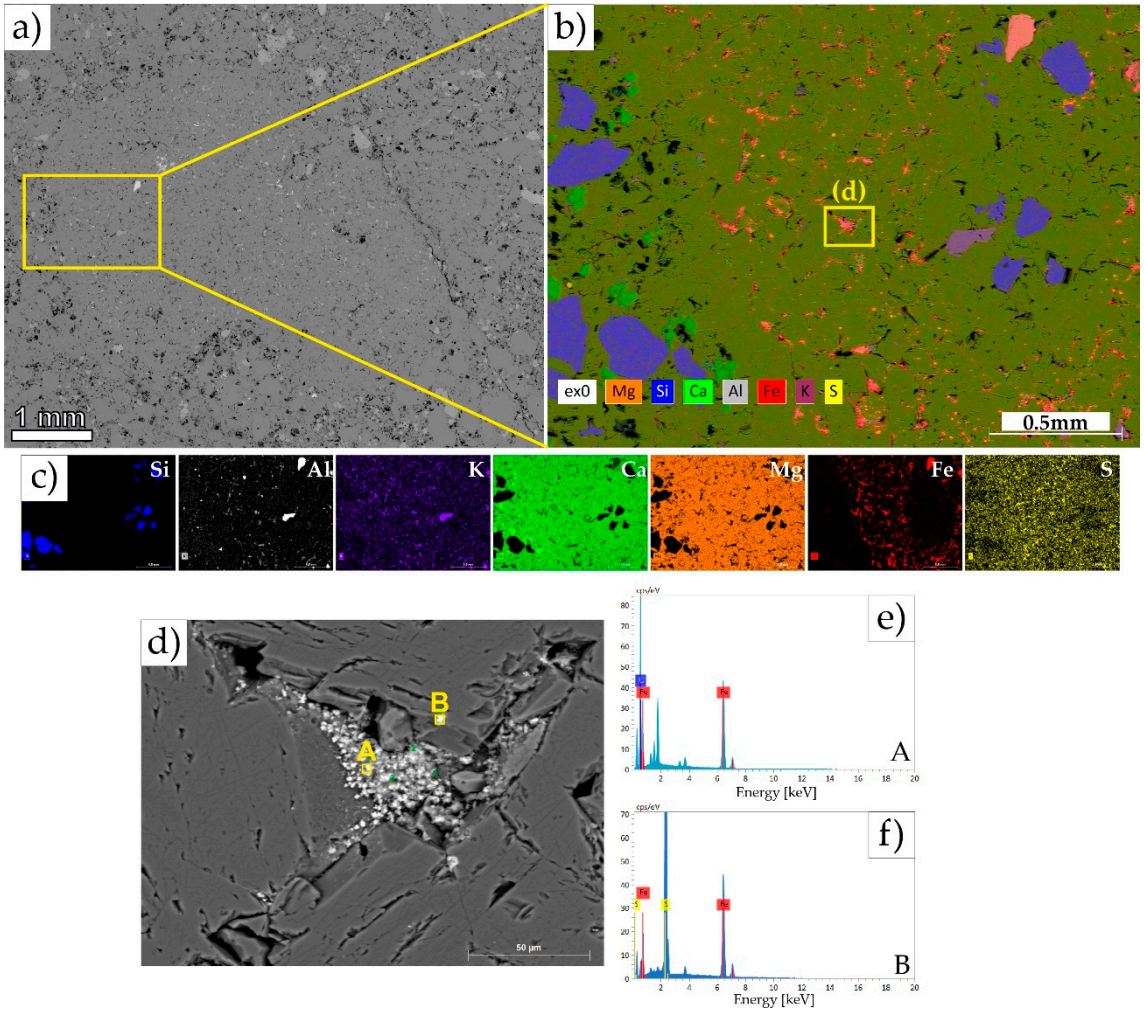

Figure S7. SEM-EDS analysis of the Fe-bearing grains in the thick section of MCSF04. (a) BSE mosaic showing the location of the SEM-EDS map (yellow box). (b) Composite element map; the yellow box marks the area shown in (d). (c) Individual element maps (same scale as b). (d) BSE image of an intercrystalline pore filled by Fe-rich grains, with analysed points A and B. (e, f) EDS spectra of points A (Fe-O, no S) and B (Fe-S). SEM-EDS analyses were carried out at CETEM with a Zeiss Sigma 300 VP field-emission SEM under high vacuum at 20 kV, on carbon-coated sections, with a backscattered-electron detector and a Bruker Quantax 400 EDS system with two XFlash 6|60 silicon drift detectors (60 mm² each).